

Article

Thermoelectric Performance Optimization of n-Type $\text{La}_{3-x}\text{Sm}_x\text{Te}_4/\text{Ni}$ Composites via Sm Doping

Jian Li ^{1,2}, Qingfeng Song ¹, Ruiheng Liu ³, Hongliang Dong ⁴, Qihao Zhang ^{1,2}, Xun Shi ¹, Shengqiang Bai ^{1,2,*} and Lidong Chen ^{1,2}

HPSTAR
1406-2022

¹ State Key Laboratory of High Performance Ceramics and Superfine Microstructure, Shanghai Institute of Ceramics, Chinese Academy of Sciences, Shanghai 200050, China; lijian1@student.sic.ac.cn (J.L.); qfsong@mail.sic.ac.cn (Q.S.); zhangqh@mail.sic.ac.cn (Q.Z.); xshi@mail.sic.ac.cn (X.S.); cld@mail.sic.ac.cn (L.C.)

² Center of Materials Science and Optoelectronics Engineering, University of Chinese Academy of Sciences, Beijing 100049, China

³ Institute of Advanced Materials Science and Engineering, Shenzhen Institutes of Advanced Technology, Chinese Academy of Sciences, Shenzhen 518055, China; rh.liu@siaat.ac.cn

⁴ Center for High Pressure Science and Technology Advanced Research, Shanghai 201203, China; hongliang.dong@hpstar.ac.cn

* Correspondence: bsq@mail.sic.ac.cn; Tel.: +86-21-6916-3532

Abstract: La_3Te_4 -based rare-earth telluride is a kind of n-type high-temperature thermoelectric (TE) material with an operational temperature of up to 1273 K, which is a promising candidate for thermoelectric generators. In this work, the Sm substitution in $\text{La}_{3-x}\text{Sm}_x\text{Te}_4/\text{Ni}$ composites is reported. The electrical transport property of $\text{La}_{3-x}\text{Sm}_x\text{Te}_4$ is modified by reducing carrier concentration due to the substitution of Sm^{2+} for La^{3+} . The electric thermal conductivity decreases by 90% due to carrier concentration reduction, which mainly contributes to a reduction in total thermal conductivity. Lattice thermal conductivity also decreases by point-defect scattering by Sm doping. Meanwhile, based on our previous study, compositing nickel improves the thermal stability of the $\text{La}_{3-x}\text{Sm}_x\text{Te}_4$ matrix. Finally, combined with carrier concentration optimization and the decreased thermal conductivity, a maximum zT of 1.1 at 1273 K and an average zT_{ave} value of 0.8 over 600 K–1273 K were achieved in $\text{La}_{2.315}\text{Sm}_{0.685}\text{Te}_4/10 \text{ vol.}\% \text{ Ni}$ composite, which is among the highest TE performance reported in La_3Te_4 compounds.

Keywords: thermoelectric; lanthanum telluride; carrier concentration optimization; composite



Citation: Li, J.; Song, Q.; Liu, R.; Dong, H.; Zhang, Q.; Shi, X.; Bai, S.; Chen, L. Thermoelectric Performance Optimization of n-Type $\text{La}_{3-x}\text{Sm}_x\text{Te}_4/\text{Ni}$ Composites via Sm Doping. *Energies* **2022**, *15*, 2353. <https://doi.org/10.3390/en15072353>

Academic Editor: Bertrand Lenoir

Received: 24 February 2022

Accepted: 21 March 2022

Published: 23 March 2022

Publisher's Note: MDPI stays neutral with regard to jurisdictional claims in published maps and institutional affiliations.



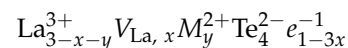
Copyright: © 2022 by the authors. Licensee MDPI, Basel, Switzerland. This article is an open access article distributed under the terms and conditions of the Creative Commons Attribution (CC BY) license (<https://creativecommons.org/licenses/by/4.0/>).

1. Introduction

Thermoelectric (TE) materials can convert heat into electricity directly, which have been applied in radioisotope thermoelectric generators (RTGs) used for deep space exploration for over half-century or in generators for waste heat recovery in industry and the human body [1–5]. In thermoelectric generators (TEGs), the thermal-to-electricity conversion efficiency of TE devices (η_{TE} ($\eta_{\text{TE}} = \frac{T_{\text{H}} - T_{\text{C}}}{T_{\text{H}}} \frac{\sqrt{1 + zT}}{\sqrt{1 + zT} + \frac{T_{\text{C}}}{T_{\text{H}}}}$) is mainly determined by Carnot efficiency η_{Carnot} ($\eta_{\text{Carnot}} = (T_{\text{H}} - T_{\text{C}})/T_{\text{H}}$) and the dimensionless figure of merit (zT) of TE materials [6,7]. $zT = S^2\sigma T/\kappa$, where S , σ , T , and κ are the Seebeck coefficient, electrical conductivity, absolute temperature, and thermal conductivity, respectively [8–11]. High service temperature and the large temperature differences will benefit energy conversion efficiency. Thus, research in high-temperature TE materials has advanced significantly in the last decades, and several promising materials have been discovered [12,13]. Thereinto, lanthanum telluride ($\text{La}_{3-x}\text{Te}_4$) promotes energy conversion efficiency up to 15% in the segment couple-level prototype, roughly doubling the heritage technologies of traditional SiGe alloys [14,15].

$\text{La}_{3-x}\text{Te}_4$ possesses a Th_3P_4 -type structure (space group $I-43d$). In the last decades, the thermoelectric properties and mechanical properties of $\text{La}_{3-x}\text{Te}_4$ have been studied due to their potential applications in RTGs [16–18]. When changing lanthanum vacancies, the electronic behavior of $\text{La}_{3-x}\text{Te}_4$ varies from metallic at $x = 0$ (La_3Te_4) to the semi-insulating at $x = 1/3$ (La_2Te_3). When $0 \leq x < 1/3$, $\text{La}_{3-x}\text{Te}_4$ exhibits n-type conducting behavior, and its carrier concentration can be widely tuned by controlling the La vacancies [19]. Additionally, $\text{La}_{3-x}\text{Te}_4$ exhibits intrinsically low lattice thermal conductivity due to its complex crystal structure, which leads to the strong electron–phonon scattering by high carrier concentrations and the strong point-defect scattering relative to phonons by vacancies. Therefore, the introduction of La vacancy is an effective method to optimize the carrier concentration and further improve the TE performance of $\text{La}_{3-x}\text{Te}_4$. For example, the high zT of 1.1 at 1273 K of $\text{La}_{3-x}\text{Te}_4$ with the optimum carrier concentration $n \sim 9 \times 10^{20} \text{ cm}^{-3}$ is obtained via stoichiometry control [15]. The nanocomposite strategy also benefits the thermoelectric performance enhancement for $\text{La}_{3-x}\text{Te}_4$ and other materials in recent years [20,21].

In addition to La vacancy regulation, it has been demonstrated that non-isoelectronic substitution is also a powerful method to tune the carrier concentration via creating vacancy-free structures, allowing for a relatively independent impact on the lattice thermal conductivity of various defects (vacancies and substitutional atoms) in the La sub-lattice and electron–phonon interactions [22]. The substitutions in the $\text{La}_{3-x}\text{Te}_4$ system either on La^{3+} sites (by Yb^{2+} , Ca^{2+} , etc.) or on Te^{2-} sites (by Sb^{3-} , Bi^{3-} , etc.) have been explored to optimize the carrier concentration in recent years [22–24]. In the case of cation substitutions on La^{3+} sites, the substitution of a divalent cation M^{2+} for La^{3+} ($\text{La}_{3-x-y}M_y\text{Te}_4$) results in an electronic local environment of the following:



with a theoretical carrier concentration of $n = n_{\text{max}} (1 - 3x - y)$, which can obtain a threefold improvement in the control of carrier concentrations. For instance, non-rare earth dopant Ca^{2+} modified the density of states to improve the power factor and achieved a finer control over the carrier concentration. A $zT_{\text{max}} \sim 1.2$ at 1273 K was obtained for $\text{La}_{2.2}\text{Ca}_{0.78}\text{Te}_4$ with an optimum carrier concentration of $1.1 \times 10^{21} \text{ cm}^{-3}$ [22]. A peak zT of ~ 1.2 at 1273 K was obtained at the carrier concentration of $n \sim 0.3 \times 10^{21} \text{ cm}^{-3}$ by substituting Yb^{2+} for La^{3+} [23].

For this study, samarium was chosen as the dopant due to Sm^{2+} (122 pm) being similar in ionic size with La^{3+} (103.2 pm), which improves the probability of successful substitution upon the La site, which is expected to reduce the high carrier concentration in La_3Te_4 . In addition, there is a possibility that Sm may exist in the form of mixed valence state $\text{Sm}^{2+}/\text{Sm}^{3+}$. Nakahara et al. revealed the mixed $\text{Sm}^{2+}/\text{Sm}^{3+}$ substitution on the La^{3+} site in the $\text{La}_{3-y}\text{Sm}_y\text{S}_4$ system [25], and the valence fluctuation of Sm also exists in Sm_3Te_4 system [26]. Thus, this observation encourages us to understand the effect of Sm element doping on the electrical and thermal transport properties in lanthanum telluride.

Here, we propose a strategy to enhance the TE performance of $\text{La}_{3-x}\text{Sm}_x\text{Te}_4$ by doping with samarium (Sm). When the Sm content is above 0.65, the coexistence of Sm^{2+} and Sm^{3+} ions in $\text{La}_{3-x}\text{Sm}_x\text{Te}_4$ is experimentally confirmed by an X-ray absorption spectrum (XAS). The substitution of La^{3+} by Sm^{2+} results in a decrease in carrier concentration and modifies the electrical properties. Moreover, the decrease in carrier concentration greatly reduces the electric thermal conductivity (κ_e), and Sm substitution on La^{3+} can also introduce point defects to strengthen phonon scattering and further reduce lattice thermal conductivity (κ_L). The composited metallic Ni inclusions are used to improve thermal stability and oxidation resistance, as proved in our previous work [27]. Consequently, an enhanced zT value of 1.1 at 1273 K and an average zT_{ave} value of 0.8 over 600 K–1273 K were obtained in $\text{La}_{2.315}\text{Sm}_{0.685}\text{Te}_4/\text{Ni}$ composites.

2. Materials and Methods

A series of $\text{La}_{3-x}\text{Sm}_x\text{Te}_4/10 \text{ vol.}\% \text{ Ni}$ composite ($x = 0, 0.4, 0.6, 0.65, 0.685, 0.69, 0.7$) samples was synthesized by the melting–ball milling–hot pressing method. The weighted chunks of La (Alfa Aesar, 99.9%), Sm (Alfa Aesar, 99.9%), and Te (Alfa Aesar, 99.999%) elements were loaded into a carbon crucible and sealed in evacuated quartz tubes. The sealed quartz tube was then heated at 1373 K for 15 h, followed by furnace cooling to room temperature. The melted ingot was ball milled in a stainless-steel vial (MSK-SFM-3) for 3 h at 1400 rpm to obtain the $\text{La}_{3-x}\text{Sm}_x\text{Te}_4$ powders. Then, the 10 vol.% metallic Ni (Alfa Aesar, 99.9%, 1–5 μm) powders were mixed in with the $\text{La}_{3-x}\text{Sm}_x\text{Te}_4$ powders by using the ball milling process once more. The $\text{La}_{3-x}\text{Sm}_x\text{Te}_4/\text{Ni}$ bulks were sintered by hot pressing at 1400 K under 80 MPa for 90 min. To avoid oxidation, the processes of raw material weighing, quartz tube sealing, powder loading, and ball milling were performed in a glove box under an argon atmosphere.

The phase structure was determined by Powder X-ray Diffraction (PXRD, Bruker, Cu $K\alpha$: $\lambda = 1.5406 \text{ \AA}$). The morphology and microstructure were observed using scanning electron microscopy (SEM, ZEISS Supra 55). Element distributions were characterized using energy dispersive spectroscopy (EDS). The electrical conductivity (σ) and Seebeck coefficient (S) were measured by an electrical measurement system (SBA458, Netzsch: Bayern, Germany) under a helium atmosphere. Thermal diffusivity (D) was measured by laser flash system (LFA457, Netzsch: Bayern, Germany), and the specific heat capacity (C_p) was taken from previously published specific heat capacity results that were modified to add samarium content following the Dulong–Petit law [27]. Then, thermal conductivity (κ) was calculated by $\kappa = \rho \times C_p \times D$, where ρ is the measured density. The Hall coefficient (R_H) was measured under a magnetic field of -3 T to 3 T with a five-probe configuration using a Physical Property Measurement System (PPMS, Quantum Design). All samples should be preserved in a glove box under an inert atmosphere before and after testing.

3. Results and Discussion

Figure 1a shows the PXRD patterns of the as-synthesized $\text{La}_{3-x}\text{Sm}_x\text{Te}_4$ ($x = 0, 0.4, 0.6, 0.65, 0.685, 0.69, 0.7$)/10 vol.% Ni composites. The main phase can be indexed relative to the Th_3P_4 -type structure ($I-43d$, ICSD-642044) of La_3Te_4 . The major peaks shift gradually to lower angles with the increase in Sm content from 0 to 0.65, indicating the expansion of the lattice. There is no obvious shift for the peaks with Sm content between 0.65 and 0.7. Some diffraction peaks belonging to the cubic structure of Ni ($Fm-3m$, ICSD-41508) are also found. Very weak diffraction peaks near 30° belonging to the impurity phases of $\text{La}_2\text{O}_2\text{Te}$ are commonly observed due to the presence of trace oxidation [23]. The calculated average crystalline size of $\text{La}_{3-x}\text{Sm}_x\text{Te}_4/\text{Ni}$ composites is 93.2 nm by using the Debye–Scherrer equation [28]. Taking the as-synthesized $\text{La}_{2.4}\text{Sm}_{0.6}\text{Te}_4/10 \text{ vol.}\% \text{ Ni}$ composite, for example, the SEM image and EDS elemental mapping are shown in Figure 1b. All elements, La, Sm, and Te, are homogeneously distributed inside the matrix. The XRD pattern and SEM-EDS results indicated that Sm atoms successfully replaced La atoms into the lattice. The fine Ni particles (smaller than 5 μm) are also well dispersed in the sample. The solubility limit of Sm is not explored fully in La_3Te_4 because the further reduction in carrier concentration is not conducive to the TE properties of lanthanum telluride.

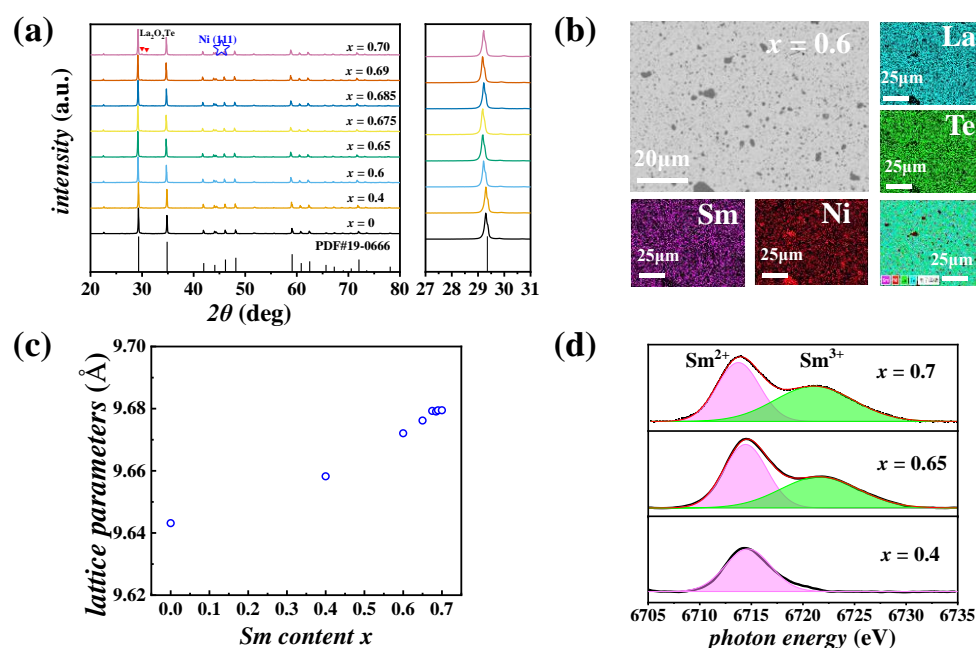


Figure 1. (a) PXRD patterns of the as-synthesized $\text{La}_{3-x}\text{Sm}_x\text{Te}_4$ ($x = 0, 0.4, 0.6, 0.65, 0.675, 0.685, 0.69, 0.7$)/10 vol.% Ni composites. (b) Backscattered electron microscopy (BSE) image and elemental mappings for the as-synthesized $\text{La}_{2.4}\text{Sm}_{0.6}\text{Te}_4$ /10 vol.% Ni. (c) Lattice parameters of as-synthesized $\text{La}_{3-x}\text{Sm}_x\text{Te}_4$ as a function of Sm content. (d) XAS spectra of $\text{La}_{2.6}\text{Sm}_{0.4}\text{Te}_4$, $\text{La}_{2.35}\text{Sm}_{0.65}\text{Te}_4$, and $\text{La}_{2.3}\text{Sm}_{0.7}\text{Te}_4$ composited with 10 vol.% Ni.

To better understand the crystal structure evolution of $\text{La}_{3-x}\text{Sm}_x\text{Te}_4$, the Rietveld refinement (Fullprof) is performed based on the PXRD patterns of Figure 1a. The cubic lattice parameters ($a = b = c$) as a function of the Sm content x are presented in Figure 1c. It is noted that the lattice parameters increase discontinuously with a break near $x = 0.65$ and then remain the same, which is a coincidence with the shift of diffraction peaks in Figure 1a. As known, samarium and tellurium can form an inhomogeneous mixed-valence compound Sm_3Te_4 with the Th_3P_4 -type structure, where Sm^{2+} and Sm^{3+} coexist with mixed valence [26]. Thus, it suggests that the valence fluctuation of Sm can be the main reason for the nonlinear change of the lattice parameters in $\text{La}_{3-x}\text{Sm}_x\text{Te}_4$ samples.

To address the issue of the evolution of Sm valence states with Sm content x , the XAS spectra at the Sm L_3 -edge are displayed in Figure 1d for $\text{La}_{2.6}\text{Sm}_{0.4}\text{Te}_4$, $\text{La}_{2.35}\text{Sm}_{0.65}\text{Te}_4$, and $\text{La}_{2.3}\text{Sm}_{0.7}\text{Te}_4$ composited with 10 vol.% Ni samples. For the sample with $x = 0.4$, only a single peak was observed at 6714 eV, corresponding to the divalent Sm (Sm^{2+}) [29,30]. Confining attention to $x = 0.65$ and $x = 0.7$ samples, two distinct peaks, separated by the same energy difference of about 8 eV, were found in the XAS spectra. This unambiguously evidences the mixed-valence character of Sm since the high-energy peak at 6722 eV corresponds to the trivalent Sm (Sm^{3+}) [29,30]. In addition, the intensity of the high-energy peak is regularly enhanced with increasing Sm content x without an energy shifts. This demonstrates that the Sm^{3+} content gradually increases with increasing Sm content x . However, it is difficult to quantify the content of Sm^{2+} and Sm^{3+} accurately because Sm^{2+} could be an oxidation relative to Sm^{3+} in the sample's surface during the etching process before measurements [31]. The XAS spectra infer that the coexistence of $\text{Sm}^{2+}/\text{Sm}^{3+}$ when Sm content x is above ~ 0.65 . Sm^{2+} doped on La^{3+} sites result in an increase in lattice parameters due to the radius of Sm^{2+} (122 pm) being larger than that of La^{3+} (103.2 pm). Sm^{3+} appears in these samples when Sm content x is above ~ 0.65 . The difference of the radius between Sm^{3+} (95.8 pm) and Sm^{2+} causes the lattice parameters to deviate from the linear change with increasing Sm content (see Figure 1c).

Figure 2a,b show the temperature dependence of electrical conductivity σ and Seebeck coefficient S for all our samples. The negative S indicates that all our samples are n-type conduction dominated by electrons. σ decreases with an increase in temperature, showing the typical behavior of heavily doped semiconductors. With increasing Sm content x , a significant reduction in σ is observed throughout the entire measured temperature range. σ for the sample with $x = 0.69$ is $\sim 3.95 \times 10^4 \text{ S m}^{-1}$ at 300 K, only about 10% of that for the sample with $x = 0$. Unlike σ , the absolute value of S increases with increasing Sm content x . The absolute value of S for the sample with $x = 0.69$ is $\sim 256 \mu\text{V K}^{-1}$ at 1000 K, over triple of the value for the sample with $x = 0$. Interestingly, for these samples with large Sm content x , the absolute value of S decreases with increasing temperature at elevated temperatures due to minority carrier activation. For the samples with low Sm content x , the absolute value of S increases linearly with increasing temperatures. A similar behavior was observed in Yb-doped $\text{La}_{3-x}\text{Te}_4$, reported by May [23].

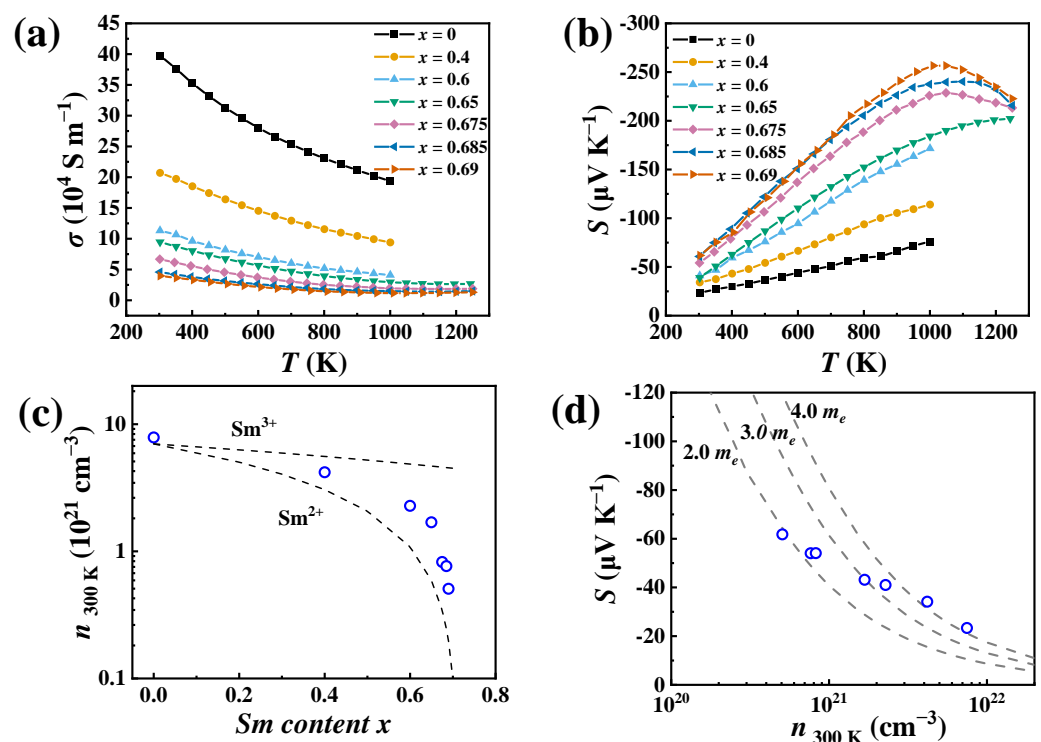


Figure 2. Temperature dependence of (a) electrical conductivity σ ; (b) Seebeck coefficient S for the $\text{La}_{3-x}\text{Sm}_x\text{Te}_4/10 \text{ vol.}\% \text{ Ni}$ composites ($x = 0, 0.4, 0.6, 0.65, 0.675, 0.685, 0.69$). (c) Room temperature Hall carrier concentration $n_{300\text{K}}$ as a function of Sm content x . The black dashed lines represent the theoretical carrier concentration calculated from nominal composition with Sm^{2+} and Sm^{3+} doping, respectively. (d) Room temperature S as a function of $n_{300\text{K}}$ for all samples. The gray dashed lines are calculated by the single parabolic band model with different effect masses m^* ($2.0 m_e, 3.0 m_e$, and $4.0 m_e$).

To further investigate the influence of Sm on σ and S , the room temperature Hall carrier concentration $n_{300\text{K}}$ as a function of Sm content x is given in Figure 2c. Assuming that all Sm are Sm^{2+} or Sm^{3+} , the expected carrier concentration is also presented for the nominal Sm-doped samples (the black dashed lines in Figure 3c). As expected, $n_{300\text{K}}$ decreases with increasing Sm content due to the additional holes created by the substitution of Sm^{2+} for La^{3+} . The $n_{300\text{K}}$ for the sample with $x = 0.69$ is $\sim 0.5 \times 10^{21} \text{ cm}^{-3}$, about one-twelfth of that for the pristine sample. The carrier concentration for all samples falls in the middle of two expected lines and follows the trend of the expected Sm^{2+} line. It is inferred that the average valence of Sm is closer to Sm^{2+} , which plays a major role in optimizing carrier concentrations.

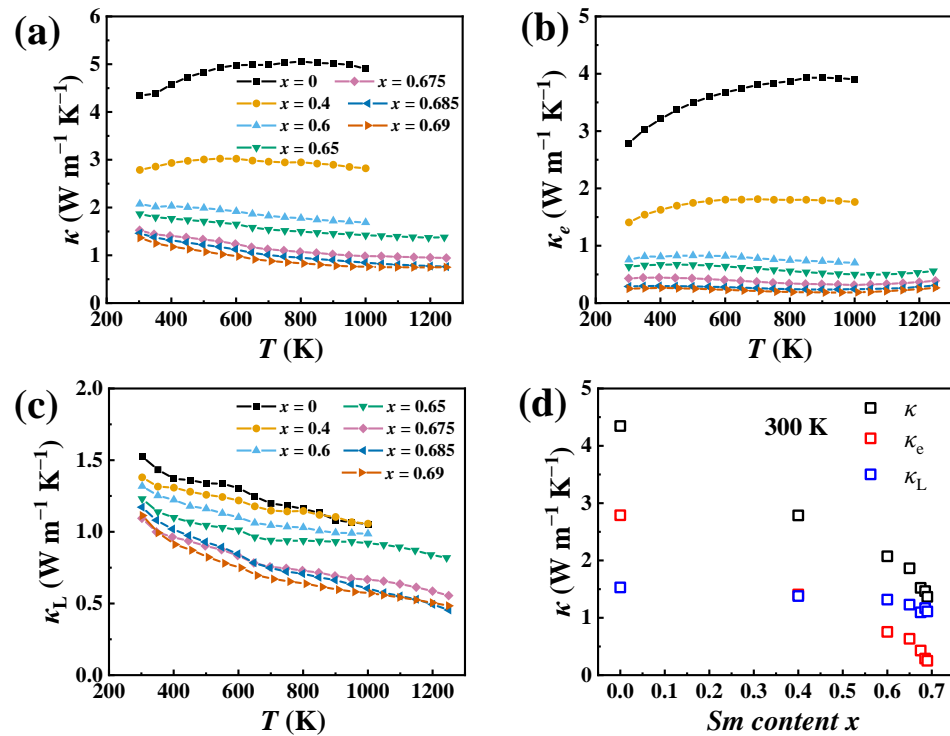


Figure 3. Temperature dependence of (a) total thermal conductivity κ_{total} , (b) electric thermal conductivity κ_e , and (c) lattice thermal conductivity κ_L for $\text{La}_{3-x}\text{Sm}_x\text{Te}_4$ ($x = 0, 0.4, 0.6, 0.65, 0.675, 0.685, 0.69$)/10 vol.% Ni composites. (d) Room temperature κ_{total} , κ_e , and κ_L as a function of the Sm content for all samples.

The Pisarenko relations calculated by the parabolic band model with the different effect mass m^* ($2.0 m_e$, $3.0 m_e$, and $4.0 m_e$) are plotted in Figure 2d. The effect mass m^* of all samples is between $2.0 m_e$ and $4.0 m_e$, which agrees with previous works [15,32]. Notably, the data for these samples with low Sm content ($x < 0.6$) fall well on the gray dashed line generated by the parabolic band model with $m^* = 4.0 m_e$, indicating that these samples possess similar m^* . For the samples with large Sm content ($x > 0.6$), m^* decreases from $4.0 m_e$ to $2.0 m_e$ with increasing Sm content. Therefore, Sm content not only affects carrier concentrations but also affects band structure.

Figure 3a shows the temperature dependence of the total thermal conductivity, κ_{total} , for all samples. As expected, κ_{total} decreases with increasing Sm content. The samples with large Sm content demonstrate low κ_{total} values of less than $1 \text{ W m}^{-1} \text{ K}^{-1}$ at 1200 K. κ_{total} in a solid usually consists of two parts. One is the electric thermal conductivity, κ_e , which can be calculated using the Wiedemann–Franz law $\kappa_e = \sigma LT$ (where σ is the electrical conductivity, L is the Lorenz number, and T is the absolute temperature). Here, L is calculated by the following approximation: $L = 1.5 + \exp(-|S|/116)$ [33]. The other one is the lattice thermal conductivity, κ_L , obtained by subtracting κ_e from κ_{total} . Figure 3b,c present κ_e and κ_L for all our samples. Similarly to κ_{total} , κ_e and κ_L also decrease with increasing Sm content. To more clearly depict the influence on thermal conductivity by Sm doping, κ_{total} , κ_e , and κ_L at 300 K are provided in Figure 3d. κ_e decreases from 2.85 to $0.25 \text{ W m}^{-1} \text{ K}^{-1}$ with increasing Sm content from $x = 0$ to 0.69 at 300 K due to a reduction in σ according to the Wiedemann–Franz law, which mainly contributes to the reduction in κ_{total} . In addition to κ_e , κ_L also decreases from 1.5 to $1.1 \text{ W m}^{-1} \text{ K}^{-1}$ at 300 K with increasing Sm content.

In order to further understand the role of Sm-doping on thermal transport, we model the low-temperature κ_L data for $\text{La}_{2.315}\text{Sm}_{0.685}\text{Te}_4/10 \text{ vol.}\% \text{ Ni}$ composites. Three phonon scattering mechanisms are considered in this study, including the Umklapp process (U), grain boundaries (B), and point defects (PD). Detailed calculations can be found in the Supplementary Materials. The contributions from different phonon scattering mechanisms

to κ_L are shown in Figure S1a. The κ_L at low temperature is greatly suppressed by grain boundaries, while its effect can be neglected above 50 K. When point-defect scatterings are involved, the calculated curve fits well with the experimental data. This illustrates that the point-defect scattering introduced by Sm substitution contributes to κ_L reduction. In addition, the role of different phonon scattering mechanisms can be more clearly reflected by the spectral lattice thermal conductivities (κ_S) for the sample with $x = 0.685$ (shown in Figure S1b). Clearly, grain boundary scattering mainly affects the low-frequency phonons, while high-frequency phonon transfers are interrupted by point-defect scattering predominantly. By combining these three phonon scattering mechanisms, the κ_L about $0.5 \text{ W m}^{-1} \text{ K}^{-1}$ at 1273 K was obtained in $\text{La}_{2.315}\text{Sm}_{0.685}\text{Te}_4/10 \text{ vol.}\% \text{ Ni}$ composite, as observed in Figure 3b. It is noted that although Sm substitution leads to a decrease in κ_L , La vacancy doping is the most effective method for reducing κ_L in La_3Te_4 -based materials [24].

The temperature dependence of the thermoelectric figure of merit, zT , is shown in Figure 4. Due to the optimization of carrier concentration and a reduction in thermal conductivity, significantly enhanced zT s were observed. A maximal zT of about 1.1 at 1273 K is achieved in the $\text{La}_{2.315}\text{Sm}_{0.685}\text{Te}_4/10 \text{ vol.}\% \text{ Ni}$ composite, which is among the highest zT reported in La_3Te_4 compounds. For the purpose of application, the conversion efficiency of thermoelectric devices largely depends on the average figure of merit, zT_{ave} . As shown in Figure 4b, the maximum zT_{ave} of 0.8 over 600 K–1273 K in $\text{La}_{2.315}\text{Sm}_{0.685}\text{Te}_4/10 \text{ vol.}\% \text{ Ni}$ composite is obtained in this study, which is comparable to the $\text{La}_{3-x}\text{Te}_4$ -based materials reported previously in this temperature range [15,22–24].

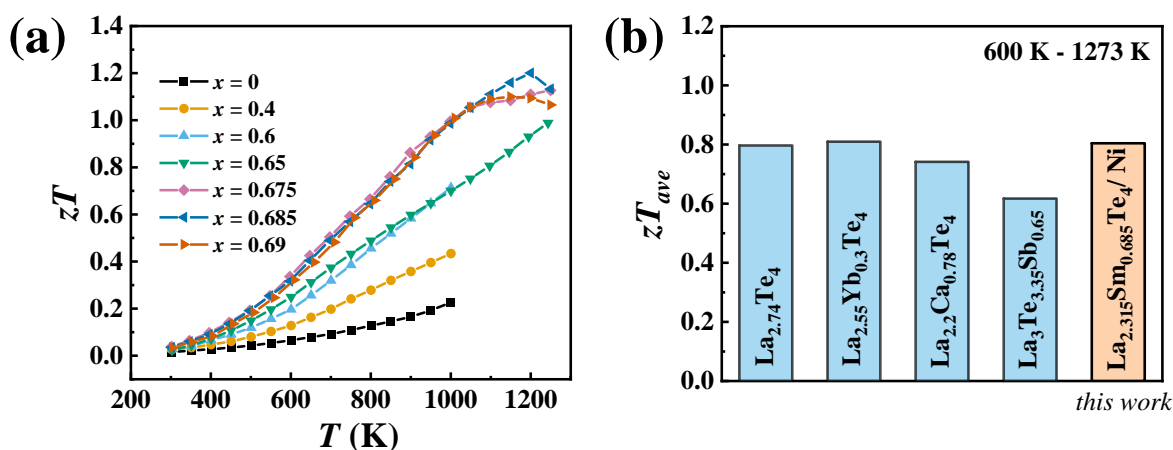


Figure 4. (a) Temperature dependence of zT for the as-synthesized $\text{La}_{3-x}\text{Sm}_x\text{Te}_4/10 \text{ vol.}\% \text{ Ni}$ composites ($x = 0, 0.4, 0.6, 0.65, 0.675, 0.685, 0.69$). (b) Comparison of the average zT_{ave} with optimized hall carrier concentration for $\text{La}_{2.315}\text{Sm}_{0.685}\text{Te}_4/\text{Ni}$ composite and for the reported $\text{La}_{3-x}\text{Te}_4$ matrix [15], Yb [23], Ca [22], Sb-doped [24], and La_3Te_4 -based compounds.

4. Conclusions

In this work, the successful doping of $\text{La}_{3-x}\text{Sm}_x\text{Te}_4/\text{Ni}$ composites with Sm was achieved, and the results indicate that doping with Sm is an effective strategy to improve zT for $\text{La}_{3-x}\text{Sm}_x\text{Te}_4$. Experimental results show that the substitution of the Sm can remarkably optimize carrier concentrations. Although the coexistence of $\text{Sm}^{2+}/\text{Sm}^{3+}$ is also found in $\text{La}_{3-x}\text{Sm}_x\text{Te}_4$ samples with Sm contents above ~ 0.65 , the average valence of Sm still presents closer to +2 for all samples, creating additional holes in the samples to reduce carrier concentrations and, therefore, the electric thermal conductivity. Sm substitution can also introduce point-defect scattering, leading to a reduction in lattice thermal conductivity. Due to the optimization of carrier concentrations and reductions in thermal conductivity, a maximal zT of about 1.1 at 1273 K and zT_{ave} of 0.8 over 600 K–1273 K was achieved in the $\text{La}_{2.315}\text{Sm}_{0.685}\text{Te}_4/10 \text{ vol.}\% \text{ Ni}$ composite.

Supplementary Materials: The following supporting information can be downloaded at: <https://www.mdpi.com/article/10.3390/en15072353/s1>, Figure S1: (a) Contribution from various phonon scattering mechanisms to κ_L in $\text{La}_{2.315}\text{Sm}_{0.685}\text{Te}_4/10$ vol.% Ni composite. U, B, and PD denote the Umklapp phonon–phonon process, grain boundary scattering, and point-defect scattering, respectively. (b) Calculated spectral lattice thermal conductivities κ_s for $\text{La}_{2.315}\text{Sm}_{0.685}\text{Te}_4/10$ vol.% Ni composite at 300 K.; Table S1: Fitting results obtained by the Debye–Callaway model [34–38].

Author Contributions: J.L., R.L. and H.D.: investigation; Q.S. and Q.Z.: data curation; J.L.: writing—original draft; Q.S., X.S., S.B. and L.C.: writing—review and editing. All authors have read and agreed to the published version of the manuscript.

Funding: This research was funded by the National Key Research and Development Program of China (Grant No. 2019YFB1901103), National Nature Science Foundation of China (NSFC) (Grant No. U2141208), and Key Research Program of Frontier Sciences, CAS (No. ZDBS-LY-JSC037). S. Bai acknowledges the Opening Project of State Key Laboratory of High Performance Ceramics and Superfine Microstructure (SKL202005SIC).

Institutional Review Board Statement: Not applicable.

Informed Consent Statement: Not applicable.

Data Availability Statement: The data that support the results within this paper and other findings of this study are available from the corresponding author upon reasonable request.

Acknowledgments: The X-ray absorption spectra (XAS) data of samples were collected at BL11B station of the Shanghai Synchrotron Radiation Facility (SSRF) and beamline 4B9A of the Beijing Synchrotron Radiation Facility (BSRF).

Conflicts of Interest: The authors declare no conflict of interest.

References

1. Bennett, G.L.; Rowe, D.M. *CRC Handbook of Thermoelectrics*; CRC Press: Boca Raton, FL, USA, 1995; p. 720.
2. Fleurial, J.-P.; Bux, S.; Caillat, T. Engineering of Novel Thermoelectric Materials and Devices for Next Generation, Long Life, 20% Efficient Space Power Systems. In Proceedings of the 11th International Energy Conversion Engineering Conference, San Jose, CA, USA, 15–17 July 2013; p. 3927.
3. Meng, F.; Chen, L.; Feng, Y.; Xiong, B. Thermoelectric generator for industrial gas phase waste heat recovery. *Energy* **2017**, *135*, 83–90. [[CrossRef](#)]
4. Ando Junior, O.; Calderon, N.; de Souza, S. Characterization of a Thermoelectric Generator (TEG) System for Waste Heat Recovery. *Energies* **2018**, *11*, 1555. [[CrossRef](#)]
5. Yang, S.; Qiu, P.; Chen, L.; Shi, X. Recent Developments in Flexible Thermoelectric Devices. *Small Sci.* **2021**, *1*, 2100005. [[CrossRef](#)]
6. Zoui, M.A.; Bentouba, S.; Stocholm, J.G.; Bourouis, M. A Review on Thermoelectric Generators: Progress and Applications. *Energies* **2020**, *13*, 3606. [[CrossRef](#)]
7. Hooshmand Zaferani, S.; Jafarian, M.; Vashae, D.; Ghomashchi, R. Thermal Management Systems and Waste Heat Recycling by Thermoelectric Generators—An Overview. *Energies* **2021**, *14*, 5646. [[CrossRef](#)]
8. Zhang, Q.; Bai, S.; Chen, L. Technologies and Applications of Thermoelectric Devices: Current Status, Challenges and Prospects. *J. Inorg. Mater.* **2019**, *34*, 279.
9. Bu, Z.; Zhang, X.; Hu, Y.; Chen, Z.; Lin, S.; Li, W.; Xiao, C.; Pei, Y. A record thermoelectric efficiency in tellurium-free modules for low-grade waste heat recovery. *Nat. Commun.* **2022**, *13*, 237. [[CrossRef](#)]
10. Bu, Z.; Zhang, X.; Hu, Y.; Chen, Z.; Lin, S.; Li, W.; Pei, Y. An over 10% module efficiency obtained using non-Bi₂Te₃ thermoelectric materials for recovering heat of <600 K. *Energy Environ. Sci.* **2021**, *14*, 6506–6513. [[CrossRef](#)]
11. Zhao, K.; Zhu, C.; Qiu, W.; Yang, S.; Su, H.; Qiu, P.; He, Y.; Guan, M.; Wei, T.-R.; Ma, J.; et al. Novel meta-phase arising from large atomic size mismatch. *Matter* **2022**, *5*, 605–615. [[CrossRef](#)]
12. Liu, W.; Kim, H.S.; Jie, Q.; Ren, Z. Importance of high power factor in thermoelectric materials for power generation application: A perspective. *Scr. Mater.* **2016**, *111*, 3–9. [[CrossRef](#)]
13. Sparks, T.D.; Gaultois, M.W.; Oliynyk, A.; Brgoch, J.; Meredig, B. Data mining our way to the next generation of thermoelectrics. *Scr. Mater.* **2016**, *111*, 10–15. [[CrossRef](#)]
14. Hendricks, T.J. *Thermoelectric Generator Energy Harvesting Research at NASA-JPL-Where We Are Now and Where We Can Go: Thermoelectric Materials and Systems-From Basic Science to Applications*; McMaster Institute of Energy Studies, McMaster University: Hamilton, ON, Canada, 2016.
15. May, A.F.; Fleurial, J.-P.; Snyder, G.J. Thermoelectric performance of lanthanum telluride produced via mechanical alloying. *Phys. Rev. B* **2008**, *78*, 125205. [[CrossRef](#)]

16. May, A.F.; Singh, D.J.; Snyder, G.J. Influence of band structure on the large thermoelectric performance of lanthanum telluride. *Phys. Rev. B* **2009**, *79*, 153101. [[CrossRef](#)]
17. Delaire, O.; May, A.F.; McGuire, M.A.; Porter, W.D.; Lucas, M.S.; Stone, M.B.; Abernathy, D.L.; Ravi, V.A.; Firdosy, S.A.; Snyder, G.J. Phonon density of states and heat capacity of $\text{La}_{3-x}\text{Te}_4$. *Phys. Rev. B* **2009**, *80*, 184302. [[CrossRef](#)]
18. Ma, J.M.; Firdosy, S.A.; Kaner, R.B.; Fleurial, J.-P.; Ravi, V.A. Hardness and fracture toughness of thermoelectric $\text{La}_{3-x}\text{Te}_4$. *J. Mater. Sci.* **2013**, *49*, 1150–1156. [[CrossRef](#)]
19. Wang, Y.; Chong, X.; Hu, Y.-J.; Shang, S.-L.; Drymiotis, F.R.; Firdosy, S.A.; Star, K.E.; Fleurial, J.-P.; Ravi, V.A.; Chen, L.-Q.; et al. An alternative approach to predict Seebeck coefficients: Application to $\text{La}_{3-x}\text{Te}_4$. *Scr. Mater.* **2019**, *169*, 87–91. [[CrossRef](#)]
20. Cheikh, D. Synthesis and Characterization of Rare-Earth Tellurides and Their Composites for High Temperature Thermoelectric Applications. Ph.D. Thesis, University of California, Los Angeles, CA, USA, 2017.
21. Karim, A.V.; Hassani, A.; Eghbali, P.; Nidheesh, P.V. Nanostructured modified layered double hydroxides (LDHs)-based catalysts: A review on synthesis, characterization, and applications in water remediation by advanced oxidation processes. *Curr. Opin. Solid State Mater. Sci.* **2022**, *26*, 100965. [[CrossRef](#)]
22. Ma, J.M.; Clarke, S.M.; Zeier, W.G.; Vo, T.; Von Allmen, P.; Snyder, G.J.; Kaner, R.B.; Fleurial, J.P.; Bux, S.K. Mechanochemical synthesis and high temperature thermoelectric properties of calcium-doped lanthanum telluride $\text{La}_{3-x}\text{Ca}_x\text{Te}_4$. *J. Mater. Chem. C* **2015**, *3*, 10459–10466. [[CrossRef](#)]
23. May, A.F.; Fleurial, J.-P.; Snyder, G.J. Optimizing Thermoelectric Efficiency in $\text{La}_{3-x}\text{Te}_4$ via Yb Substitution. *Chem. Mater.* **2010**, *22*, 2995–2999. [[CrossRef](#)]
24. May, A.F.; Flage-Larsen, E.; Snyder, G.J. Electron and phonon scattering in the high-temperature thermoelectric $\text{La}_3\text{Te}_{4-z}\text{M}_z$ ($M = \text{Sb, Bi}$). *Phys. Rev. B* **2010**, *81*, 125205. [[CrossRef](#)]
25. Nakahara, J.F.; Takeshita, T.; Tschetter, M.J.; Beaudry, B.J.; Gschneidner, K.A. Thermoelectric properties of lanthanum sulfide with Sm, Eu, and Yb additives. *J. Appl. Phys.* **1988**, *63*, 2331–2336. [[CrossRef](#)]
26. Boucherle, J.-X.; Givord, F.; Schweizer, J.; Gukasov, A.; Mignot, J.-M.; vre-Berna, E.L.; Aoki, H.; Ochiai, A. Polarized neutron investigation in the mixed-valence compound Sm_3Te_4 . *Phys. B* **1999**, *267*, 37–40. [[CrossRef](#)]
27. Li, J.; Liu, R.; Song, Q.; Gao, Z.; Huang, H.; Zhang, Q.; Shi, X.; Bai, S.; Chen, L. Enhanced thermal stability and oxidation resistance in $\text{La}_{3-x}\text{Te}_4$ by compositing metallic nickel particles. *Acta Mater.* **2021**, *224*, 117526. [[CrossRef](#)]
28. Eghbali, P.; Hassani, A.; Sündü, B.; Metin, Ö. Strontium titanate nanocubes assembled on mesoporous graphitic carbon nitride ($\text{SrTiO}_3/\text{mpg-C}_3\text{N}_4$): Preparation, characterization and catalytic performance. *J. Mol. Liq.* **2019**, *290*, 111208. [[CrossRef](#)]
29. Mizumaki, M.; Tsutsui, S.; Iga, F. Temperature dependence of Sm valence in SmB_6 studied by X-ray absorption spectroscopy. *J. Phys. Conf. Ser.* **2009**, *176*, 012034.
30. Yoshikane, N.; Matsui, K.; Nakagawa, T.; Terzidou, A.G.V.; Takabayashi, Y.; Yamaoka, H.; Hiraoka, N.; Ishii, H.; Arvanitidis, J.; Prassides, K. Pressure-induced valence transition in the mixed-valence $(\text{Sm}_{1/3}\text{Ca}_{2/3})_{2.75}\text{C}_{60}$ fulleride. *Mater. Chem. Front.* **2020**, *4*, 3521–3528. [[CrossRef](#)]
31. Sousanis, A.; Poelman, D.; Detavernier, C.; Smet, P.F. Switchable Piezoresistive SmS Thin Films on Large Area. *Sensors* **2019**, *19*, 4390. [[CrossRef](#)]
32. Gomez, S.J.; Cheikh, D.; Vo, T.; Von Allmen, P.; Lee, K.; Wood, M.; Snyder, G.J.; Dunn, B.S.; Fleurial, J.-P.; Bux, S.K. Synthesis and Characterization of Vacancy-Doped Neodymium Telluride for Thermoelectric Applications. *Chem. Mater.* **2019**, *31*, 4460–4468. [[CrossRef](#)]
33. Kim, H.-S.; Gibbs, Z.M.; Tang, Y.; Wang, H.; Snyder, G.J. Characterization of Lorenz number with Seebeck coefficient measurement. *APL Mater.* **2015**, *3*, 041506. [[CrossRef](#)]
34. Cahill, D.G.; Watson, S.K.; Pohl, R.O. Lower limit to the thermal conductivity of disordered crystals. *Phys. Rev. B Condens. Matter.* **1992**, *46*, 6131–6140. [[CrossRef](#)]
35. Callaway, J. Model for Lattice Thermal Conductivity at Low Temperatures. *Phys. Rev.* **1959**, *113*, 1046–1051. [[CrossRef](#)]
36. Callaway, J.; von Baeyer, H.C. Effect of Point Imperfections on Lattice Thermal Conductivity. *Phys. Rev.* **1960**, *120*, 1149–1154. [[CrossRef](#)]
37. Yang, J.; Meisner, G.P.; Chen, L. Strain field fluctuation effects on lattice thermal conductivity of ZrNiSn-based thermoelectric compounds. *Appl. Phys. Lett.* **2004**, *85*, 1140–1142. [[CrossRef](#)]
38. Holland, M.G. Phonon Scattering in Semiconductors From Thermal Conductivity Studies. *Phys. Rev.* **1964**, *134*, A471–A480. [[CrossRef](#)]